Journal of Materials Science & Technology 211 (2025) 72–81

Contents lists available at ScienceDirect

Journal of Materials Science & Technology

journal homepage: www.elsevier.com/locate/jmst

Research Article

Revelling pore microstructure impacts on the compressive strength of porous proppant based on finite and discrete element method

Zijia Liao[a,c], Hesamoddin Rabiee[b], Lei Ge[b,*], Xiaogang Li[c,*], Zhaozhong Yang[c], Qi Xue[c], Chao Shen[a], Hao Wang[b,*]

[a] Tianfu Yongxing Laboratory, Chengdu, 610213, China
[b] Centre for Future Materials, University of Southern Queensland, Springfield, QLD, 4300, Australia
[c] State Key Laboratory of Oil and Gas Reservoir Geology and Exploitation, Southwest Petroleum University, Chengdu, 610500, China

ARTICLE INFO

Article history:
Received 1 December 2023
Revised 26 April 2024
Accepted 2 May 2024
Available online 18 June 2024

Keywords:
Porous proppant
Finite and discrete element method (FDEM)
Crack
Compressive strength

ABSTRACT

Ceramic spheres, typically with a particle diameter of less than 0.8 mm, are frequently utilized as a critical proppant material in hydraulic fracturing for petroleum and natural gas extraction. Porous ceramic spheres with artificial inherent pores are an important type of lightweight proppant, enabling their transport to distant fracture extremities and enhancing fracture conductivity. However, the focus frequently gravitates towards the low-density advantage, often overlooking the pore geometry impacts on compressive strength by traditional strength evaluation. This paper numerically bypasses such limitations by using a combined finite and discrete element method (FDEM) considering experimental results. The mesh size of the model undergoes validation, followed by the calibration of cohesive element parameters via the single particle compression test. The stimulation elucidates that proppants with a smaller pore size (40 μm) manifest crack propagation evolution at a more rapid pace in comparison to their larger-pore counterparts, though the influence of pore diameter on overall strength is subtle. The inception of pores not only alters the trajectory of crack progression but also, with an increase in porosity, leads to a discernible decline in proppant compressive strength. Intriguingly, upon crossing a porosity threshold of 10 %, the decrement in strength becomes more gradual. A denser congregation of pores accelerates crack propagation, undermining proppant robustness, suggesting that under analogous conditions, hollow proppants might not match the strength of their porous counterparts. This exploration elucidates the underlying mechanisms of proppant failure from a microstructural perspective, furnishing pivotal insights that may guide future refinements in the architectural design of porous proppant.

1. Introduction

Ceramic spheres have found a wide array of applications in various industries due to their unique properties. These spheres, characterized by their high strength and thermal stability, have become increasingly vital in fields such as filtration, catalysis, and thermal insulation [1–9]. One of the most noteworthy applications of ceramic spheres is in the domain of hydraulic fracturing, where they are utilized as proppants. Hydraulic fracturing stands as a prevalent stimulation technique employed to amplify the production of fluids from subterranean formations. Within this process, pressurized fluid is forcefully injected into reservoirs to create fractures. To hold the fractures open, propping agents (proppant particles) are mixed with the fluid and injected into the formations, as shown in Fig. 1 [10,11]. The basic proppant types include sand and ceramic. Sand has been used as proppant particles since hydraulic fracturing was first successfully tested in 1947 [12,13]. Sand, in general, constitutes a robust, abrasion-resistant, and chemically stable silicate mineral, derived from the crushing and screening of quartz. The apparent density of sand approximates 2.65 g/cm^3. Beyond a closure stress of 20 MPa, sand commences breaking [14–16]. In contrast, ceramic proppant is crafted from sintered bauxite, kaolin, magnesium silicate, or blends of bauxite and kaolin [17–20]. In comparison to quartz sand, ceramic proppant boasts superior strength and density [21,22]. Ideally, proppant particles should exhibit lower density, facilitating their transportation to the end of fractures, particularly for hydraulic fracturing of shale or coal to form multiple fractures. However, compared to fracturing fluid, the

* Corresponding authors.
E-mail addresses: lei.ge@usq.edu.au (L. Ge), lixiaogang@swpu.edu.cn (X. Li), hao.wang@usq.edu.au (H. Wang).

https://doi.org/10.1016/j.jmst.2024.05.054

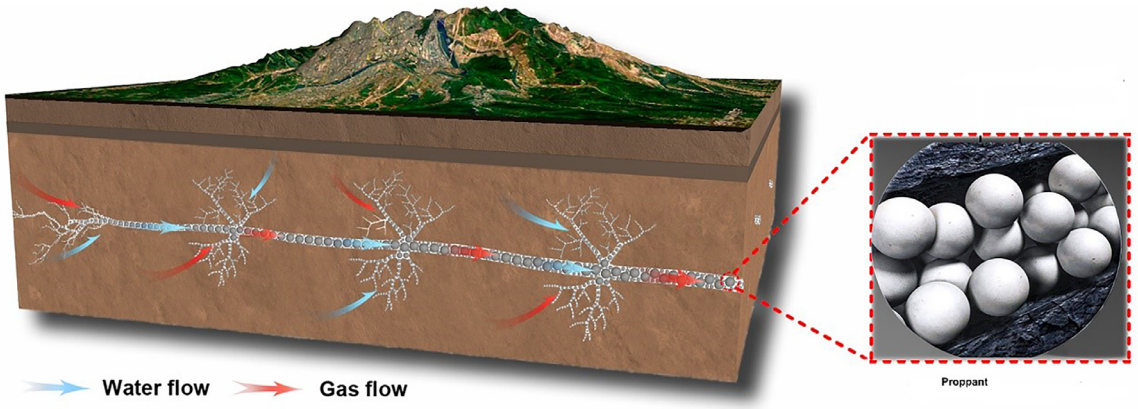

Fig. 1. Illustration of hydraulic fracturing and the role of proppant [11].

density of quartz sand or ceramic proppant proves excessive, posing challenges in effectively filling remote fractures [23–25]. Consequently, low-density porous proppants have garnered exceptional attention [26,27].

Over recent years, various techniques have been employed to impart porous structure to proppants, resulting in a significant reduction in their overall density. For example, Fan et al. [28] reported a noteworthy case wherein a porous proppant boasting an exceptionally low apparent density of 1.25 g/cm^3 was introduced. This specific proppant was synthesized from low-grade bauxite, nano-silica, micro-silica, and sodium metasilicate by instant sintering through thermal plasma and closed-external pore sintering using a rotary kiln. Urbanek et al. [29] proposed an economically efficient method for manufacturing porous proppant with apparent density ranging from 1.0 to 2.9 g/cm^3, involving the preparation of ceramic precursor material, dispersion in low-temperature boiling liquid, creation of particles with liquid-filled pores, drying to remove pores, and final sintering into generally spherical particles, marking a significant innovation in porous proppant production. Optimal proppant should possess not only low density but also a requisite level of compressive strength [30–32]. The proppant with insufficient compressive strength is prone to succumb under high closure stress, resulting in disintegration and the generation of fines or fragments. This diminishes the permeability of the fracture created by hydraulic fracturing and consequently impacts its effectiveness. However, there is often an excessive focus on the density of porous proppant, while the impact of increased pores on proppant strength tends to be overlooked. Previous studies have demonstrated that pores play a significant role in influencing particle strength. For example, Savchenko et al. [33] experimentally observed porous alumina ceramics when subjected to deformation by compression. It was shown that the destruction process was controlled by shearing stresses. The size and location of damages depend on the pore space volume. Serkova et al. [34] presented the digital analysis of reconstructed 3D micro-CT images for studying the internal voids and the pore distribution inside the proppant. The findings revealed that proppant strength depends on its porosity rather than the pore distribution. Keleş et al. [35] proposed a two-dimensional finite element model to assess the pore–pore interactions on fracture statistics of porous material. The study revealed that even at extremely low porosity levels, such as 2 %, these pore-to-pore interactions remain significant for compressive strength.

In the literature, there exists a significant gap in quantitative analysis on the correlation of pore geometry with the mechanical properties of proppant. Therefore, in this study, we provide a comprehensive analysis of the impact of pore size, porosity, and pore distribution on the crack patterns and compressive strength of porous proppant utilizing the finite and discrete element method (FDEM). This represents the first application of FDEM in this field. This study enriches the research on porous proppant and holds significant implications for the lightweight proppant industry.

2. Experiment and method

In this section, two samples (marked as sample A and sample B) of ceramic proppant (40/70 mesh, 0.212 to 0.425 mm) were obtained from Panzhihua Bing Yang Technology Co Ltd. Comprehensive tests were conducted on their density, strength, and microstructure. The information on materials and tests used in this work is listed in Fig. S1 in Supplementary Information. The experimental results can provide parameters for modeling and verification.

2.1. Density and crushing tests

Density tests for proppants include measurements of bulk density and apparent density. Strength assessments involve compressive strength levels and single-particle compression tests. The protocols for evaluating the bulk density, apparent density, and compressive strength level follow the guidelines specified in SY/T5108-2014 [36]. The steps of the single-particle compression test are listed in Supplementary Information.

2.2. Microstructure measurement

The microstructure of the ceramic proppant was determined by X-ray diffraction (XRD), scanning electron microscopy (SEM), and porosity test, providing a basis for explaining the performance of the ceramic proppant. Phase identification was performed using XRD (X'Pert Pro, Malvern panalytical) with Cu Kα radiation at a scanning rate of 6.0 °/min. The pore structure of the proppant was observed using SEM (JSM-6700F, JEOL, Japan). The porosity is calculated from true density and apparent density, and its testing method is listed in the supplementary information.

3. Modeling

In this section, a combined finite and discrete element method (FDEM) approach is adopted to simulate particle breakage behavior, via multi-directional two-point loading, focusing on the pores inside proppant effects.

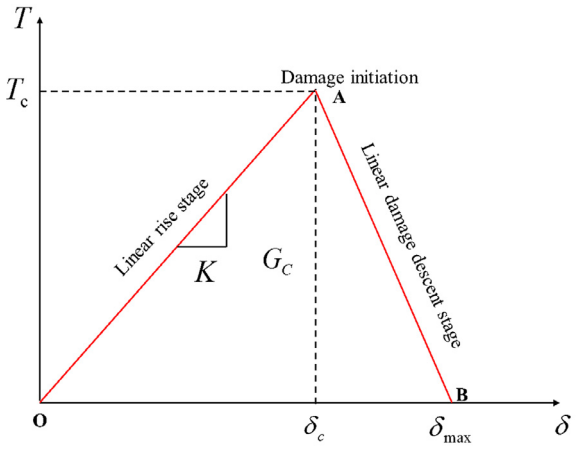

Fig. 2. Bilinear traction separation curve.

3.1. FDEM theory

The Finite Element Method (FEM) discretizes continuous systems into finite elements, enabling structural, thermal, and fluid dynamics analysis in environments with uniform materials and complex shapes. It uses local approximations within these elements to solve global equations based on continuum mechanics. In contrast, the Finite Discrete Element Method (FDEM) combines the Finite Element Method (FEM) with the Discrete Element Method (DEM), effectively simulating both the large-scale behavior of materials and the micro-scale interactions between particles. This makes FDEM ideal for addressing complex problems like crack propagation, rock mechanics, and granular material behavior, where both continuous and discrete phenomena play crucial roles [37–39]. Within the framework of FDEM, particles are discretized utilizing four-node solid tetrahedral elements in this paper, and these tetrahedral elements are linked through zero-thickness cohesive interface elements. For tetrahedral elements, the material is treated as linear-elastic using constant-strain tetrahedral elements. Cracks are caused by the failure of geometric zero-thickness cohesive elements using traction-separation damage laws. The relationship between displacement and traction force at the cohesive zone follows the bilinear function [40,41], as stated in Fig. 2. As shown in Fig. 2, T represents traction stress, δ represents opening displacement. The bilinear constitutive model can be divided into a linear rise stage (OA), a damage initiation point (A), and a linear damage descent stage (AB). Before the material reaches the stress limit, T increases linearly with the increased δ. After the material reaches the stress limit, it enters the loss stage and exhibits linear softening behavior. When δ reaches the failure strains, the cohesive element completely loses its load-bearing capacity resulting in cracks.

During the three-dimensional fracture process, there is traction stress in the normal (T_n) and two shear directions (T_s, T_t) on the crack surface. The elastic behavior before damage initiation is represented by an elastic constitutive matrix. The linear elastic behavior represented by the stiffness matrix is as follows:

$$T = \begin{Bmatrix} T_n \\ T_s \\ T_t \end{Bmatrix} = \begin{bmatrix} K_{nn} & K_{ns} & K_{nt} \\ K_{ns} & K_{ss} & K_{st} \\ K_{nt} & K_{st} & K_{tt} \end{bmatrix} \begin{Bmatrix} \delta_n \\ \delta_s \\ \delta_t \end{Bmatrix} = K\delta \tag{1}$$

where K represents the stiffness coefficient of the cohesive force element, dimensionless; T_n, T_s, T_t represents the normal stress, shear stress, and tensile stress respectively, (MPa); δ_n, δ_s, δ_t represents the normal strain, shear strain, and tensile strain, respectively.

In order to describe the damage to cohesive elements, the cohesive damage criterion selected in this paper was the quadratic nominal stress damage criterion, which can be expressed as:

$$\left(\frac{T_n}{T_N^0}\right)^2 + \left(\frac{T_s}{T_S^0}\right)^2 + \left(\frac{T_T}{T_T^0}\right)^2 = 1 \tag{2}$$

where T_N^0, T_S^0, T_T^0 represents the peak contact stress when the separation is completely perpendicular to the interface in the first and second shear directions, (MPa).

The damage evolution mode is based on the Benzeggagh Kenane criterion [42,43], and the BK fracture criterion applies to cases where the critical fracture energy is the same during deformation in two shear directions, which can be expressed as:

$$G_n^C + \left(G_S^C - G_n^C\right)\left(\frac{G_S}{G_T}\right)^2 = G^C \tag{3}$$

where G^C is the total energy release rate; G_n^C is the tensile fracture energy of the unit; G_S^C is the fracture energy when pure tensile and two shear failures occur.

3.2. Geometry and boundary conditions

In order to improve computational efficiency, this paper mainly studies the crushing behavior of a single proppant. The 3D-FDEM is developed to simulate how a porous proppant behaves when compressed by a rigid body. The following assumptions were made [44]:

(1) In the course of preparation of porous proppant, only closed pores are formed to promote its strength.
(2) Proppant and closed pores look like standard spheres.
(3) Pores do not overlap.
(4) Proppants exhibit elastic deformation.

Based on the assumption presented above, the porous proppant generation process was established by the secondary developing function of the general finite element software, as shown in Fig. 3(a). The pore generation relies on the random distribution algorithm which was validated in Section 4.2. Fig. 3(b) depicts the porous proppant model alongside the defined boundary conditions. Contact between the proppant particle and the rigid employs explicit general contact, with contact properties divided into normal and tangential components. The normal component is defined as “hard contact”, akin to contact between two rigid bodies, while the tangential component is defined by Coulomb friction. The magnitude of the tangential force is controlled by the friction coefficient, set to 0.5. Additionally, the bottom rigid body was fixed, while the top rigid body was loaded at a rate of 3 mm/s. The process of porous proppant under compression can be described dynamic explicit step. The analysis step was 0.025 s, stable time step was 7 us [45]. When the loading is finished, the relationship curve between force and displacement can be obtained. The peak load value on this curve represents the single-particle compressive strength of the proppant [46].

4. Results and discussions

4.1. Proppant characterization

Table 1 shows the density and crushing test results of two types of proppant samples. It can be seen that the proppant exhibits a maximum bulk density of 1.5 g/cm^3 and a maximum apparent density of 2.77 g/cm^3. As the classification criteria for ceramic proppants [11], the examined samples are categorized as lightweight proppants. The strength is usually correlated to the

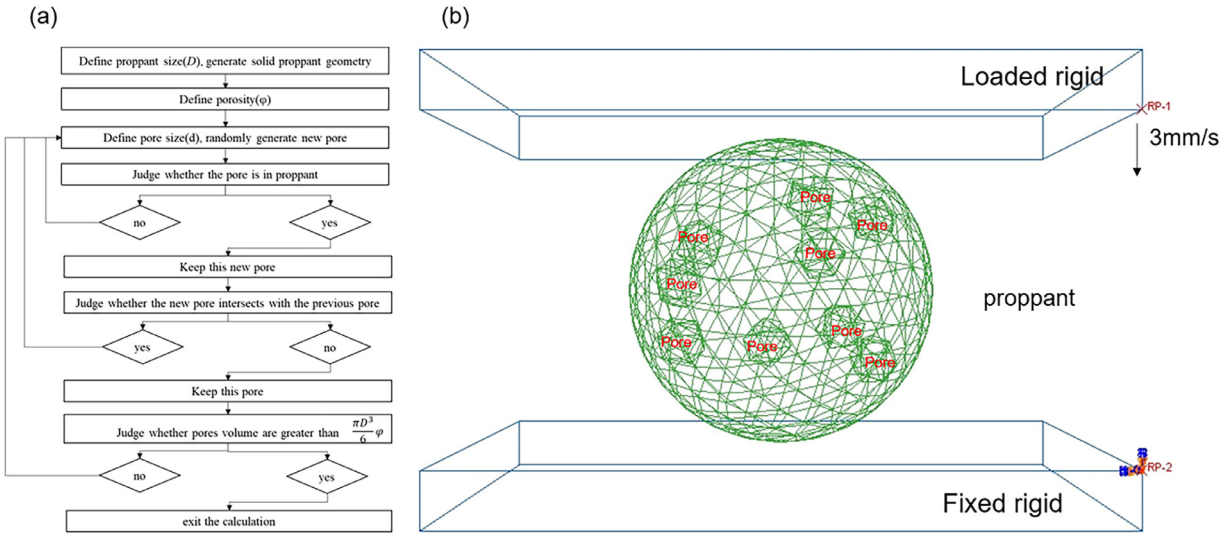

Fig. 3. Finite and discrete element Model: (a) Geometric model generation process and (b) grid and boundary model.

Table 1
The results of the proppant density and crushing test.

Sample	Bulk density (g/cm^3)	Apparent density (g/cm^3)	Compressive strength evel (MPa)	Compressive strength Value (N)
A	1.50	2.77	86	38.53
B	1.44	2.61	69	31.13

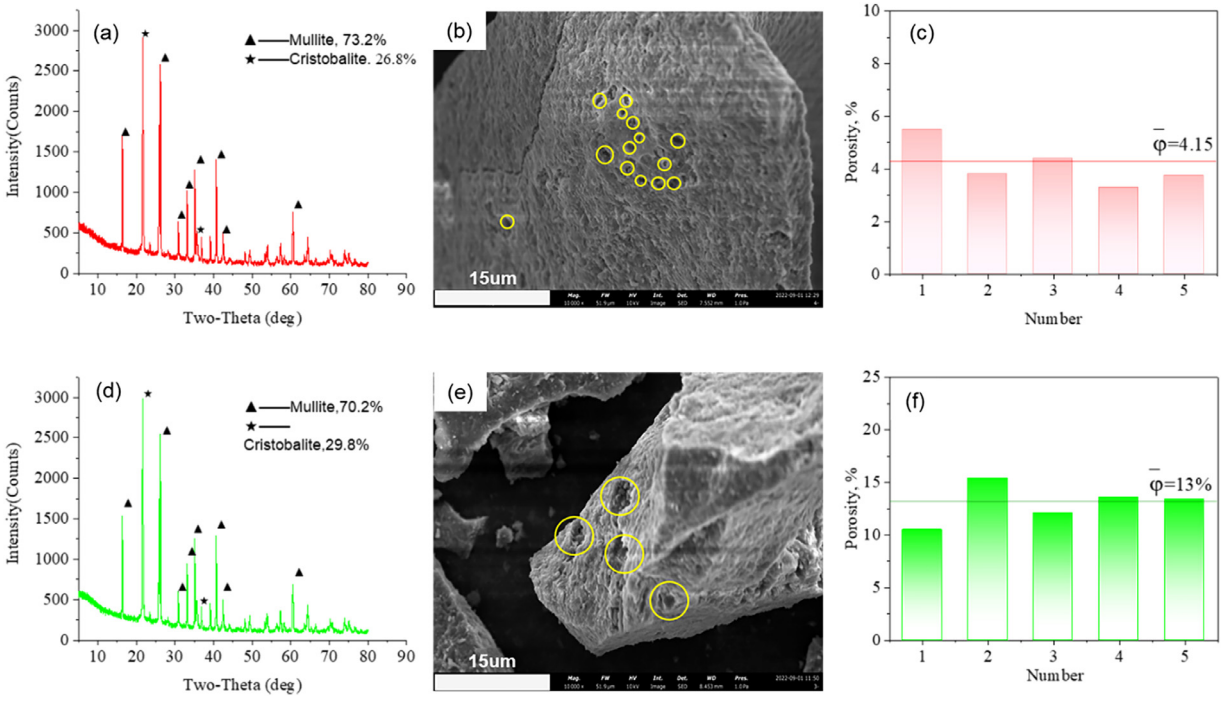

Fig. 4. The results of microstructure measurement. (a–c) Sample A, (d–f) sample B, (a, d) XRD patterns, (b, e) SEM morphology, and (c, f) repeated porosity tests.

proppant density. This distinction could potentially be attributed to variations in their microstructure.

Fig. 4 shows the microstructures of two different ceramic proppant particles. The XRD results indicate that the phase types of the two samples are the same, mainly composed of mullite and cristobalite phases. Furthermore, semi-quantitative analysis results reveal that the phase compositions of the two samples are similar. The mullite phase constitutes approximately 70 % of the content, while the quartz phase constitutes around 30 %. Mullite is a binary solid solution compound composed of Al_2O_3 and SiO_2. It remains stable at room temperature and exhibits advantages such as high-temperature resistance, resistance to acidity and alkalinity, and high mechanical strength. It is the main phase responsible for forming high-strength proppant. In cases where the phase composition and content are similar, the primary reason for the significant differences in the strength of proppant particles is the

Table 2
Basic model input parameters.

Basic geometry information	Porosity (%)	4
	Pore diameter (μm)	50
	Particle size (mm)	0.3
Material parameters of tetrahedral elements	Density (g/cm^3)	2.76
	Elastic modulus (MPa)	127,000
	Poisson's ratio	0.25
Material parameters of cohesive elements	Unit stiffness (N/mm^3)	200,000
	Unit strength (MPa)	100
	Fracture energy (N/mm)	0.25

variation in internal pore structures. Some pores identified in the cross-sectional images under SEM have been delineated using yellow circles. Both types of proppant particles exhibit distinct pore structures, predominantly in circular shape, providing a basis for the assumption of spherical pores in the FDEM. Pore analysis reveals that the porosity of Sample A is approximately 4.15 %, while that of Sample B is about 13 %. The porosity of Sample B is more than three times that of Sample A, which could be the main factor leading to the significantly lower strength of Sample B compared to A.

4.2. Validation of FDEM in simulation proppant breakage behavior

4.2.1. Basic model inputs

From Section 4.1, the lightweight ceramic proppant is mainly composed of quartz and mullite. In this study, assuming that the material of tetrahedral elements and cohesive elements is homogeneous, the theoretical elastic modulus and Poisson's ratio are calculated using the weighted average method, as follows:

$$E = \sum E_i \times V_i \tag{4}$$

$$\nu = \sum \nu_i \times V_i \tag{5}$$

where E and ν are Elastic modulus and Poisson's ratio of tetrahedral elements respectively, E_i and ν_i are the elastic modulus and Poisson's ratio of the particle phase that makes up the proppant, V_i is the volume fraction of each phase, which can be determined by XRD results.

The material parameters of tetrahedral elements are calculated according to the basic elastic parameters of quartz and mullite shown in Table S1 in Supplementary Information. The basic model input parameters are shown in Table 2.

Table 3
Designed mesh size information.

Mesh size (mm)	Number of nodes	Number of tetrahedral elements	Number of cohesive elements	Number of all elements
0.05	7352	1838	3385	5223
0.034	10,424	2606	4778	7384
0.02	21,028	5257	10,223	15,480

4.2.2. The decision on mesh size

For FDEM, crack propagation occurs along the boundaries of the elements. The choice of element size not only affects the morphology of the cracks but also has a significant impact on the computational scale. In this study, the mesh size is determined by the mechanical performance and crack morphology. Three different mesh sizes were designed for numerical simulations using the Gmsh generator. The relevant parameters are shown in Table 3.

Fig. 5 depicts the crack morphology and the displacement-load curve under different mesh sizes using basic input parameters in Table 2. Fig. 5(a) represents the crack evolution of proppant particles under different mesh sizes, with red indicating the crack locations. It can be observed that proppant particles with larger mesh sizes lead to earlier appearances of red cracks. At 0.012 s, a through crack appears for a particle with a mesh size of 0.05. At 0.015 s, the particle is penetrated by both the primary and secondary cracks. Meanwhile, for particles with mesh sizes of 0.02 and 0.034, the crack patterns are similar, with the primary crack penetrating at t = 0.015 s. From Fig. 5(b), it can be observed that as the loading process progresses, the load sustained by the proppant continues to increase. At a displacement of approximately 0.03 mm, the proppant reaches its peak load-bearing capacity, with further displacement, the load rapidly decreases, indicating that cracks have propagated. Different mesh sizes exhibit variations in their compressive strength. For proppant particles with different grid sizes, there is a small difference in their maximum load. The maximum load with a grid size of 0.05 is about 12 N, while the load with grid sizes of 0.02 and 0.034 are similar, and is about 10 N.

In numerical simulations, a smaller mesh size results in a higher number of elements, leading to more precise simulations. However, it increases computational complexity and reduces efficiency. A mesh size of 0.02 closely approximates the real state of the proppant particle but it demands a higher computational load. For example, using a dual-core processor, the computational time required for a mesh size of 0.02 approaches 30 min, while

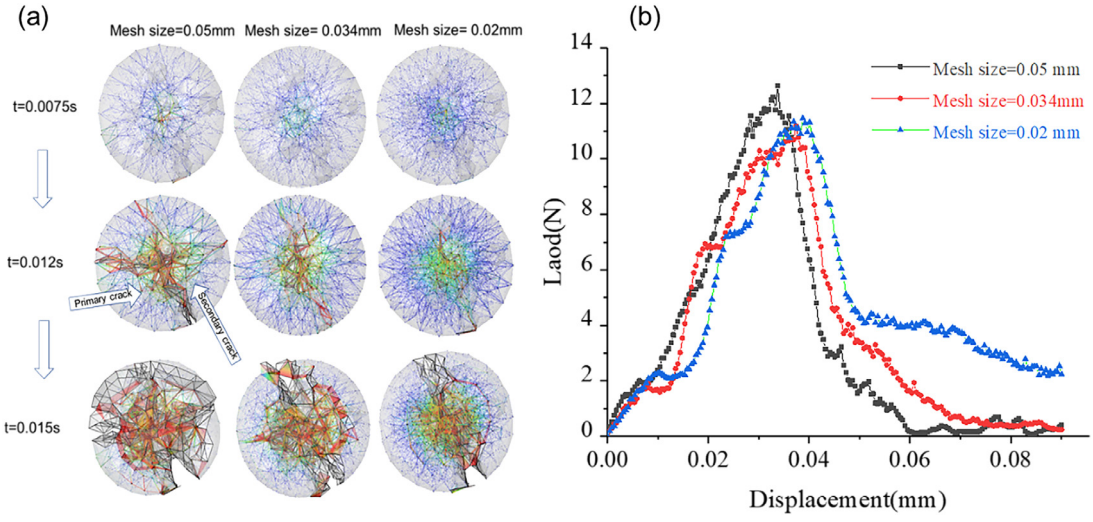

Fig. 5. Crack morphology (a) and displacement-load curve (b) under different mesh sizes.

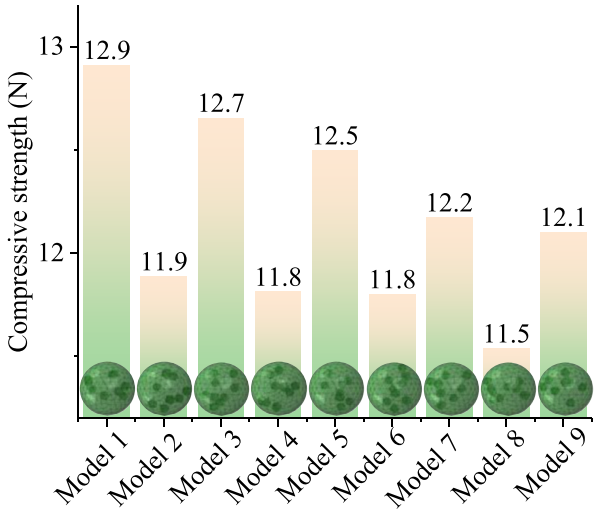

Fig. 6. Simulated compressive strength from different pore distributions in the proppants.

a mesh size of 0.034 necessitates only 10 min. Taking into account the mechanical performance and crack morphology under different mesh sizes and considering computational efficiency, a mesh size of 0.034 is chosen, as it balances both mechanical performance and fracture patterns.

4.2.3. Validation of pore generation method

Owing to the random distribution employed in the pore generation method, variations in proppant strength may manifest even when identical parameters are utilized. To address this variability, 9 distinct models were synthesized using a randomization approach, all adhering to the identical model parameters outlined in Table 2. The computed outcomes of these models are presented in Fig. 6. It is observed that the particle compressive strength fluctuates, with a zenith of 12.9 N and a nadir of 11.5 N, yielding a maximal deviation in the vicinity of 10 %. These findings suggest that the influence of pore distribution on the compressive strength of proppant is comparatively moderate. Consequently, within the context of model computations, it is reasonable to employ a set of random distribution models as a representative under this specific pore parameter, thereby simplifying the computational process.

4.2.4. Calibration of cohesive element parameters

The calibration of the cohesive element parameters to some extent influences the simulation results. Calibration, in essence, involves continuously adjusting the cohesive element parameters of the model, comparing the simulation results from the calibrated model with experimental results, and ultimately achieving a good agreement between the numerical results and experimental results. If the calibrated macroscopic target physical quantities fall within the acceptable error range, it indicates that the model's parameter calibration is successful.

In this section, these cohesive element parameters can be calibrated through a single particle compression test in Section 2.1. Initially, based on the basic model input parameters in Table 2, we investigated the influence of cohesive element parameters on displacement-load curves. The results are shown in Fig. 7. It is evident that proppant strength increases as the cohesive element parameters are adjusted. As shown in Fig. 7(a), the unit strength increased from 50 to 400 MPa, resulting in a nearly fourfold increase in proppant strength from 6 to 22 N. From Fig. 7(b), fracture energy rises from 0.125 to 2 N/mm, leading to a twofold increase in proppant strength from 8 to 17 N. Notably, the unit strength has a more significant impact on proppant strength compared to fracture energy. From Fig. 7(c), it is evident that proppant strength remains relatively unchanged under varying unit stiffness coefficients. The stiffness primarily affects the slope during the loading process. A higher stiffness coefficient results in a steeper slope and a smaller failure displacement. For instance, a unit stiffness of 10^5 N/mm³ yields a failure displacement of approximately 0.04 mm, while a unit stiffness of 20×10^5 N/mm³ results in a smaller displacement of around 0.02 mm.

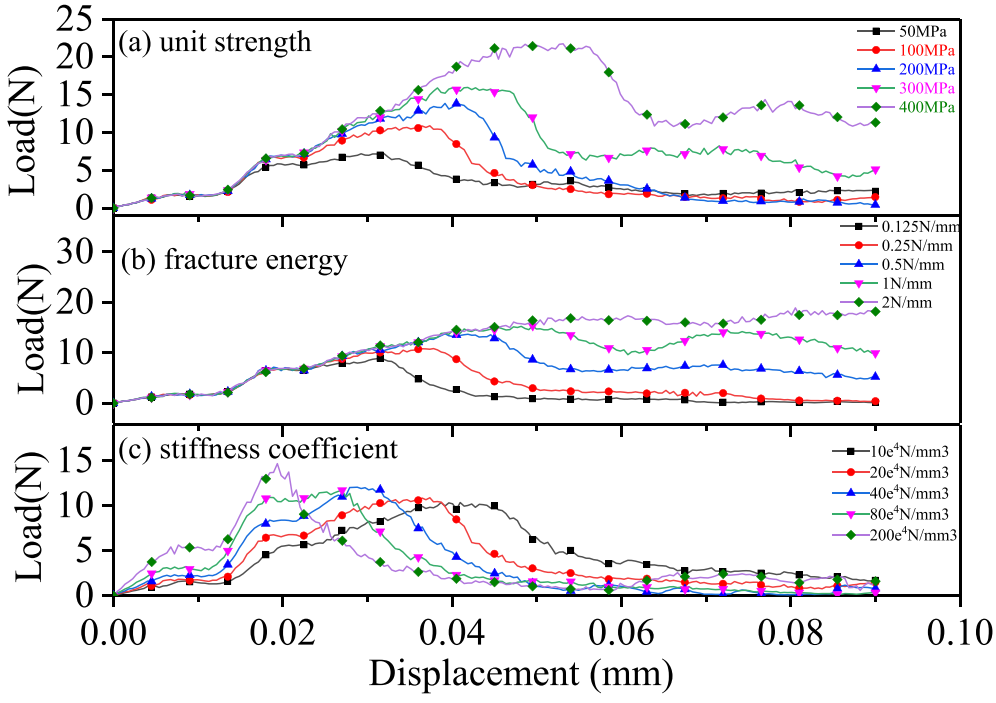

Fig. 7. The effect of cohesive element parameters on the mechanical performance: (a) unit strength, (b) fracture energy, and (c) stiffness coefficient.

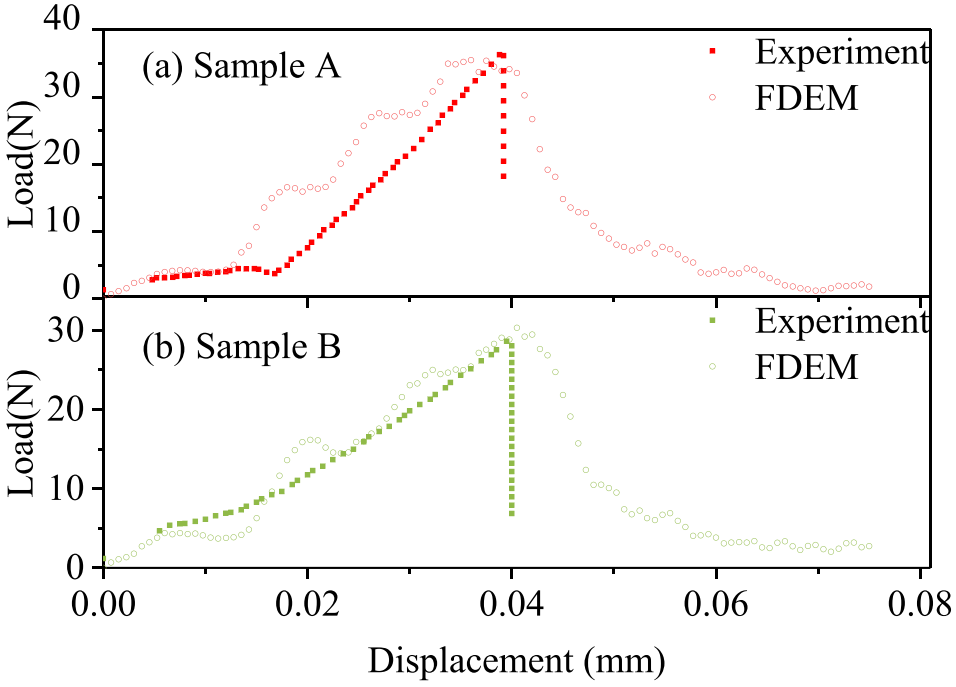

Fig. 8. Comparison between simulated and experimental results: (a) sample A and (b) sample B.

Fig. 8 presents a comparison between the simulation and the experimental results, following the adjustment of cohesive elements using the trial and error method [47]. The adjusted cohesive unit strength is set at 400 MPa, the fracture energy at 0.6 N/mm, and the unit stiffness at 120 × 10^4 N/mm³. As can be seen in Fig. 8, it's apparent that the adjusted displacement-load curve closely approximates the experimental values. However, it's worth noting the presence of multiple "small peaks" in the simulation curve before reaching the maximum load. These "small peaks" can be attributed to two primary factors. Firstly, they are a consequence of calculation oscillations due to the use of stable time steps, manifesting as a multi-peak phenomenon. Secondly, they result from the initial wear and local cracks between particles and the loading plate before the primary crack that traverses the particles emerges. These factors lead to small peaks in the displacement-load curve prior to the occurrence of fracture. Additionally, it's observable that, after reaching the maximum load, the simulation curve does not exhibit a sharp decline, as seen in the experimental curve. Instead, it displays a gradual decrease. This behavior is due to the relatively high loading rate in the simulation curve, and the presence of internal pores which influence the subsequent crushing behavior [48].

4.3. The effect of pore size on mechanical property

Pore size serves as a pivotal parameter for characterizing the structural attributes of porous proppant. Nevertheless, it is noteworthy that the existing literature addressing the influence of pore size on the mechanical strength of such porous proppant is limited. It is essential to emphasize that the pore sizes of these proppant particles are generally on the micro-meter scale. In our investigation, modified cohesion element parameters were used while keeping other parameters constant. We systematically varied the pore diameters to 40, 50, 60, and 70 μm to investigate the effects of different pore sizes on the cracks morphology and mechanical strength of the proppant. The outcomes of our simulations are presented in Fig. 9.

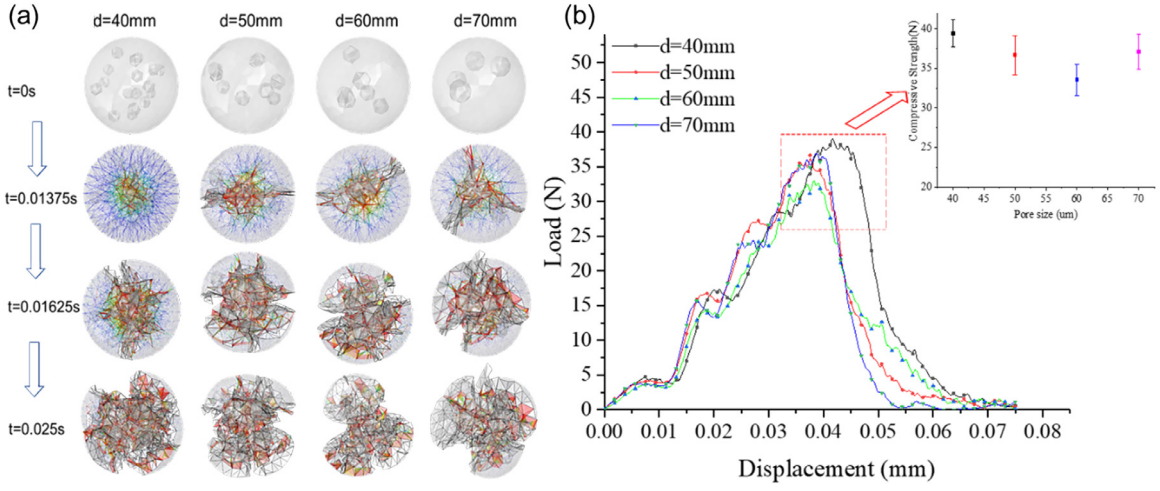

Fig. 9. Crack morphology (a) and displacement-load curve (b) under different pore sizes.

To macroscopically investigate the crack patterns of porous proppant, we have extracted crack morphology at different times, as depicted in Fig. 9(a). At 0.01375 s, proppant particles with pore sizes of 50, 60, and 70 μm have already exhibited the formation of continuous cracks, while proppant with pore size of 40 μm primarily demonstrate the development of inter-pore cracks. It is evident that, at the same time point, proppants with relatively larger pore sizes exhibit a significantly faster progression in crack expansion and evolution when contrasted with those possessing relatively smaller pore sizes. Meanwhile, at 0.025 s, proppant particles with pore sizes of 40 and 50 μm have fragmented into four smaller components, whereas proppant particles with pore sizes of 60 and 70 μm predominantly divide into three smaller segments. This observation suggests that secondary cracks are more prone to develop in proppants with smaller pore sizes in comparison to their larger pore counterparts. This phenomenon can be attributed to two primary factors: (1) Under equivalent porosity conditions, smaller pore sizes entail a higher quantity of pores distributed within the model, with smaller relative distances between these pores. When subjected to equivalent external forces, this circumstance facilitates the advancement of secondary cracks, leading to the fragmentation of the proppant into numerous smaller pieces, which subsequently affects propped fracture conductivity. (2) Under the same loading conditions, a reduced number of crack segments results in a heightened degree of stress concentration. This intensified stress concentration propels the rapid expansion of cracks, thereby accelerating crack propagation and evolution in proppants with larger pore sizes.

The impact of variations in pore size on the displacement-load relationship curve is illustrated in Fig. 9(b). This graphical representation highlights that, under equivalent porosity conditions, proppant particles with distinct pore sizes exhibit minimal disparities in their peak loads, suggesting that pore size exerts a relatively modest influence on the proppant's mechanical strength. Nevertheless, it is worth noting that for smaller pore sizes, the displacement at which the proppant attains its maximum load is notably increased, signifying a gradual material failure. This observation, in comparison to the data presented in Fig. 9, can be attributed to the fact that smaller pore sizes facilitate the formation of multiple fractures. Under identical external energy inputs, the rate of crack propagation is reduced, leading to an extended time to material failure. Moreover, when analyzing the post-peak curve, it is evident that proppants with larger pore sizes (50, 60, and 70 μm) exhibit a more rapid rate of load decay compared to those with a pore size of 40 μm, demonstrating characteristics akin to 'brittleness'.

4.4. The effect of porosity on mechanical property

Porosity stands as a fundamental characteristic in the domain of porous materials, exhibiting a profound interrelationship with structural integrity. Nonetheless, the experimental examination of the impact of porosity on the mechanical strength of proppant particles is fraught with intricacies. Furthermore, the determination of proppant strength under extreme conditions, such as when the porosity is reduced to 0 %, remains infeasible. To address this challenge, the FDEM was employed, involving the utilization of meticulously adjusted cohesion element parameters while keeping other relevant parameters consistent. This facilitated a systematic investigation of how variations in porosity ranging from 0 % to 20 %, influence the cracks morphology and mechanical characteristics of proppant.

In Fig. 10(a–d), we present the progressive development of cracks within the proppant at distinct levels of porosity, all within the confines of the same cross-sectional profile. The graphic representation underscores that differences in porosity result in divergent loci of initial crack inception within the proppant particles. As these emerging cracks propagate under the influence of external loading, the final positions of the primary macroscopic fracture lines are altered. In the instance of a pore-free proppant, cracks initiate at the upper and lower contact surfaces and proceed to swiftly propagate towards the central point of the proppant sphere. Conversely, in the case of proppant particles endowed

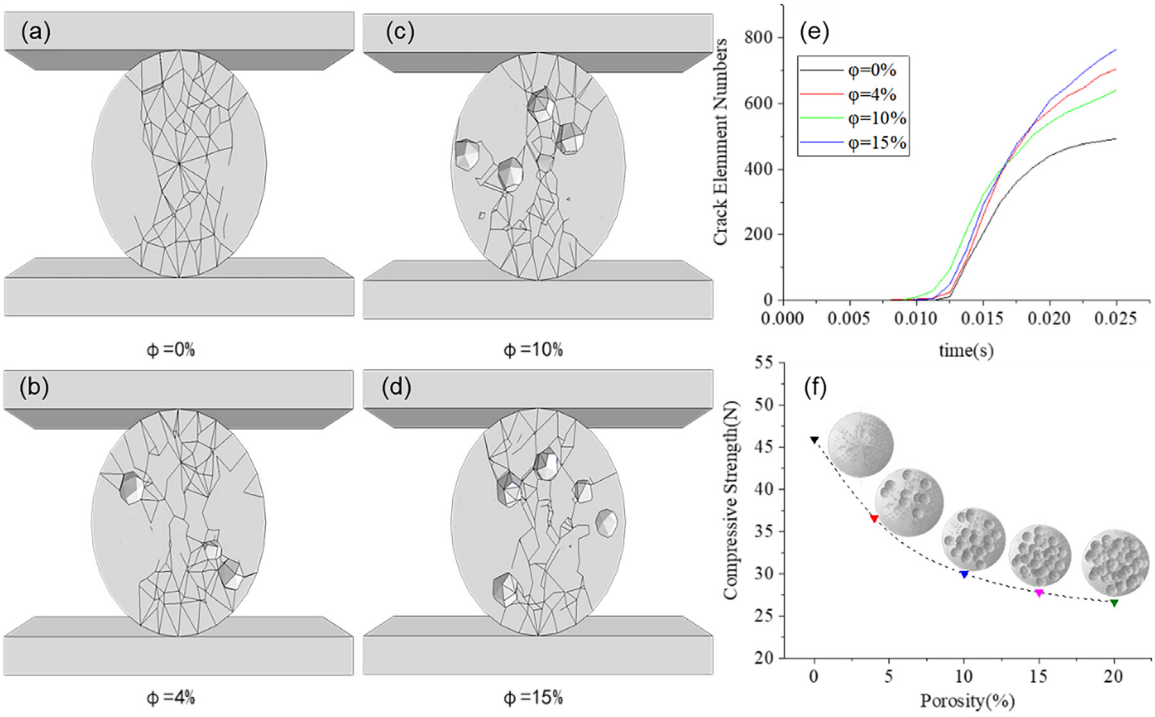

Fig. 10. Crack morphology of different porosity: (a) 0 %, (b) 4 %, (c) 10 %, and (d) 15 %. (e) The failed cohesive element numbers under different porosity. (f) Relationship between porosity and proppant compressive strength.

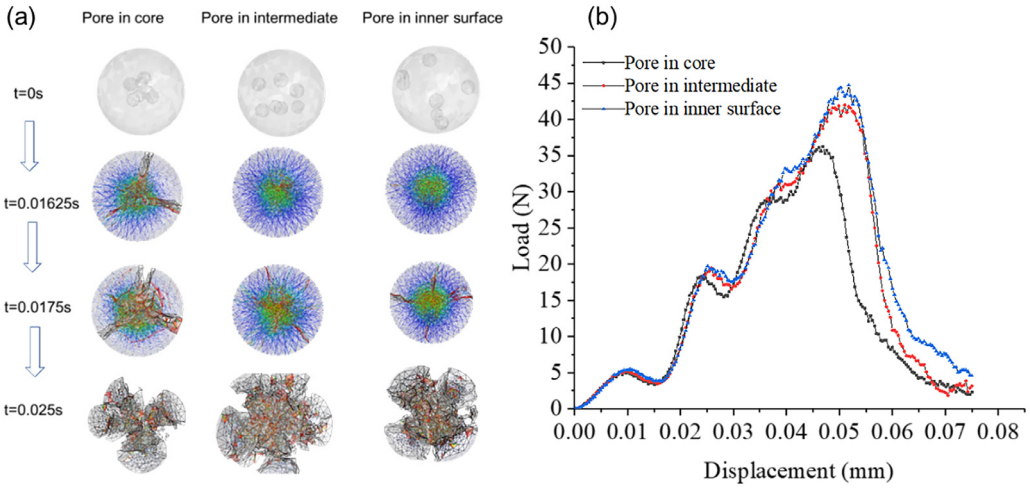

Fig. 11. Cracks morphology (a) and displacement-load curve (b) under different pore distribution cases.

with pores, the presence of these voids modulates the trajectory of crack propagation, channeling the cracks along the direction of the pores, thereby conferring increased intricacy upon the crack patterns of the porous proppant particles. Furthermore, with the passage of computational time, the numerical simulation yields valuable insight into the number of cohesive elements due to fracture, thereby serving as an indirect indicator of the degree of proppant disintegration, as shown in Fig. 10(e). A discernible trend emerges: (1) An increase in porosity is accompanied by a marked rise in the count of failed cohesive elements, indicative of a heightened propensity for crack formation and the ensuing complexities of crack morphology. (2) Cohesive elements featuring a porosity of 0 % exhibit the longest duration before experiencing failure, signifying that a diminished porosity amplifies the challenge of initiating cracks.

Fig. 10(f) offers a depiction of the compressive strength exhibited by proppant particles under varying porosity. The illustration highlights that amplification in pore volume serves to diminish the load-bearing surface area of the proppant material, resulting in a pronounced reduction in proppant strength [49]. Nevertheless, when the porosity surpasses 10 %, the variations in proppant strength exhibit a more gradual trajectory. This observation emphasizes that, relative to factors such as pore size and pore location, porosity exerts the most substantial influence on both the compressive strength of proppant particles. In the context of practical hydraulic fracturing production, proppant particles characterized by low density yet high structural toughness impart enhanced fracture conductivity. In contrast, an increase in porosity serves to reduce the proppant density and strength. Notably, when the porosity exceeds 10 %, the impact on proppant strength becomes comparatively less pronounced, thus providing invaluable guidance on the production of porous proppant particles.

4.5. The effect of pore distribution on mechanical property

The spatial distribution of pores holds great significance, as it profoundly influences the procedural details in the fabrication of porous proppant particles. Historically, porous proppant particles were crafted with a hollow configuration to mitigate their density [50–52]. In this section, employing modified cohesive element parameters and imposing a porosity of 3 %, we conducted simulations to examine the impact of diverse pore distributions—namely, within the core, intermediate, and inner surface of a spherical structure—on the compression dynamics of the porous proppant. The findings are elucidated in Fig. 11.

Fig. 11(a) shows the progression of crack formation within the proppant at various time intervals. As evidenced by Fig. 11(a), irrespective of the distinct operating conditions, the ultimate failure morphology of the proppant shares a common characteristic, characterized by its division into four primary segments. Notably, at 0.01625 s, the proppant has already manifested continuous cracks when pores are concentrated at the core, whereas in the other two scenarios, the mode of crack development predominantly involves inter-pore connectivity. This observation emphasizes the view that proppant featuring centralized pore distributions exhibits a significantly accelerated pace of crack extension and evolution. This phenomenon highlights the significance of pore distribution concentration, which facilitates faster stress propagation and thereby makes the proppant more prone to fracture.

Fig. 11(b) illustrates the displacement-load curves corresponding to various pore distribution configurations. The graph reveals a conspicuous trend wherein proppants featuring centrally concentrated pores exhibit a notably reduced strength of a mere 35 N, in contrast to those with a more widely dispersed pore distribution, which manifests a significantly elevated material strength. This observation underscores the direct relationship between support material strength and the degree of pore concentration. Particularly noteworthy is the fact that, in the context of low-density proppant particles, porous proppant outperform their hollow counterparts in terms of strength.

5. Conclusions

This study introduces the Finite-Discrete Element Method (FDEM) to investigate the crack morphology and compressive strength of porous proppant for the first time. A novel computational method for generating pore generation was developed and successfully validated. By adjusting the cohesive element parameters using displacement-load curve data from proppant crushing tests, this research evaluates the impact of pore size, porosity, and pore distribution on the mechanical properties of porous proppant. The conclusions can be concluded as follows:

(1) The pore size exerts a relatively modest influence on proppant compressive strength. Our analysis discerns distinct crack morphology across proppant particles of varied pore dimensions. It emerges that proppant particles endowed with a pore size of 40 μm experience a deceleration in crack propagation trajectories against their larger-pored counterparts.

(2) The natural occurrence of pores influences the direction of crack propagation, directing cracks to align with the orientation of the pores. This subtle interaction leads to complex crack patterns within proppant particles. At the same time, increased porosity reduces the effective load-bearing area of the proppant, resulting in a noticeable reduction in its compressive strength within a specific range. Notably, for the lightweight proppant assessed in this study, which has a mullite content of approximately 70 %, a porosity level above 10 % indicates a stabilization in the variations of proppant strength.
(3) Expanding our analytical horizon to encapsulate simulations of proppant particles characterized by variegated pore distribution spectra (encompassing core, intermediate, and inner surface), we find that the increased pore concentration accelerates stress transmission velocities. This acceleration enhances the dynamics of crack propagation within the proppant, making it more prone to fracturing, which also explains why porous proppants have greater strength than hollow proppants.

In summary, this investigation provides a novel approach to understanding porous proppant strength, offering insights that are set to drive innovation in the low-density proppant industry.

Data and materials availability

The authors declare that the data supporting the findings of this study are available within the paper and its Supporting Information.

Declaration of competing interest

We declare that we have no financial and personal relationships with other people or organizations that can inappropriately influence our work, there is no professional or other personal interest of any nature or kind in any product, service and/ or company that could be construed as influencing the position presented in, or the review of, the manuscript entitled “Revelling Pore Microstructure Impacts on the Compressive Strength of Porous Proppant Based on Finite and Discrete Element Method”.

CRediT authorship contribution statement

Zijia Liao: Writing – review & editing, Writing – original draft, Investigation, Formal analysis, Data curation. **Hesamoddin Rabiee:** Writing – review & editing. **Lei Ge:** Writing – review & editing, Writing – original draft, Supervision, Project administration, Methodology, Conceptualization. **Xiaogang Li:** Resources, Conceptualization. **Zhaozhong Yang:** Resources, Funding acquisition, Conceptualization. **Qi Xue:** Conceptualization. **Chao Shen:** Formal analysis. **Hao Wang:** Writing – review & editing, Resources, Funding acquisition, Conceptualization.

Acknowledgements

The authors acknowledge the financial support provided by Tianfu Yongxing Laboratory Organized Research Project Funding (No. 2023CXXM01) and the ARC linkage program (No. LP200100420). We are thankful for the assistance of the Tianfu Yongxing Laboratory, Southwest Petroleum University of China, University of Southern Queensland of Australia, and Panzhihua Bing Yang Technology Co Ltd for access to testing and analyzing the proppant performance.

Supplementary materials

Supplementary material associated with this article can be found, in the online version, at doi:10.1016/j.jmst.2024.05.054.

References

[1] L. Su, M. Niu, D. Lu, Z. Cai, M. Li, H. Wang, J. Mater. Sci. Technol. 75 (2021) 1–13.
[2] S. Dong, W. Han, Y. Luo, T. Zhao, C. Xu, J. Mater. Sci. Technol. 26 (2010) 228–233.
[3] Y. Liu, L. Zhang, R. Zhang, S. Shao, L. Sun, X. Wan, T. Wang, J. Mater. Sci. Technol. 155 (2023) 82–88.
[4] O.B. Apea, E.B. Akorley, E.O. Oyelude, B. Ampadu, Heliyon 9 (2023) e18343.
[5] Z. Luo, Y. Fang, M. Zhou, X. Wang, Angew. Chem.-Int. Edit. 58 (2019) 6033–6037.
[6] D. Wu, W. Li, K. Liu, Y. Yang, S. Hao, J. Mater. Sci. Technol. 106 (2022) 211–224.
[7] Y. Dong, A. Chen, T. Yang, S. Gao, S. Liu, H. Jiang, Y. Shi, C. Hu, J. Mater. Sci. Technol. 137 (2023) 247–258.
[8] C.H. Kirk, P. Wang, C.Y.D. Chong, Q. Zhao, J. Sun, J. Wang, J. Mater. Sci. Technol. 183 (2023) 152–164.
[9] X. Zhang, B. Du, P. Hu, Y. Cheng, J. Han, J. Mater. Sci. Technol. 102 (2022) 137–158.
[10] Y. Feng, C. Ma, J. Deng, X. Li, M. Chu, C. Hui, Y. Luo, Pet. Sci. 18 (2021) 807–826.
[11] Z. Liao, X. Li, L. Ge, Z. Yang, J. Zhu, Q. Xue, H. Wang, Sustain. Mater. Technol. 33 (2022) e484.
[12] M. Zborowski, J. Pet. Technol. 71 (2019) 39–41.
[13] R. Barati, J. Liang, J. Appl. Polym. Sci. 131 (2014) 40735.
[14] A. Kamel, Z. Salem, R. Chemini, M. Khodja, K. Allia, Particul. Sci. Technol. 37 (2019) 716–724.
[15] D. Knez, A. Calicki, Tech. Sci. 66 (2018) 3–8.
[16] H. Elochukwu, K.K.K. Kiat, Energy Geoscience 2 (2021) 175–180.
[17] D. Ding, Y. Fang, G. Xiao, X. Zhu, P. Fu, X. Chong, Int. J. Appl. Ceram. Tec. 18 (2021) 1832–1844.
[18] Q. Ren, Y. Ren, H. Li, X. Wu, W. Bai, J. Zheng, O. Hai, Mater. Chem. Phys. 230 (2019) 355–361.
[19] J. Zhao, Z. Liu, Y. Li, Mater. Lett. 152 (2015) 72–75.
[20] J. Hao, T. Hu, G. Cheng, B. Guo, P. Bai, Y. Tian, Mater. Res. Innov. 26 (2022) 1–7.
[21] H. Sun, B. He, H. Xu, F. Zhou, M. Zhang, H. Li, G. Yin, S. Chen, X. Xu, B. Li, ACS Omega 7 (2022) 10243–10254.
[22] R. Anaya, J.M. Martínez, M.F. Hernández, M.S. Herrea, N.M. Rendtorff, Ceram. Int. 48 (2022) 32357–32365.
[23] H. Qu, Y. Liu, H. Lin, S. Tang, R. Wang, L. Xue, Y. Hu, Int. J. Multiphas. Flow 146 (2022) 103873.
[24] H. Qu, Y. Xu, J. Hong, X. Chen, C. Li, X. Liu, Spe J. 28 (2022) 477–495.
[25] H. Qu, Y. Xu, Y. Liu, Z. Li, X. Liu, Z. Zeng, R. Guo, Energy 285 (2023) 129380.
[26] T. Chen, J. Gao, Y. Zhao, T. Liang, G. Hu, X. Han, Polymers 14 (2022) 5534.
[27] P. Liu, Q. Huang, J. Li, J. Du, X. Lu, J. Liu, C. Liu, X. Lan, Energ. Fuel 37 (2023) 3355–3370.
[28] J. Fan, T.P. Bailey, Z. Sun, P. Zhao, C. Uher, F. Yuan, M. Zhao, J. Petrol. Sci. Eng. 163 (2018) 100–109.
[29] T.W. Urbanek, Lightweight proppant and method of making same, US Patent, No. 20060016598, 2005.
[30] D. Huang, J. Wang, L. Niu, C. Zheng, J. Disper. Sci. Technol. 44 (2022) 2692–2699.
[31] X. Wei, Y. Wang, T. Yang, Y. Song, Coatings 13 (2023) 1841.
[32] W. Liu, X. Xiong, Y. Zhao, C. Liu, Y. Hou, X. Pu, Fuel 331 (2023) 125777.
[33] N. Savchenko, I. Sevostyanova, T. Sablina, L. Gömze, S. Kulkov, AIP Conf, Proc 1623 (2014) 547–550.
[34] E.P. Serkova, I.V. Safonov, I.V. Yakimchuk, J. Phys.: Conf. Ser. 1096 (2018) 12046.
[35] Ö. Keleş, R.E. García, K.J. Bowman, Acta Mater. 61 (2013) 2853–2862.
[36] W. Zhu, B. Guan, F. Cui, in: Measurement of Properties of Proppant Used in Hydraulic Fracturing and Gravel-Packing Operations, National Energy Administration, Beijing, 2014, pp. 14–17.
[37] D. Wei, B. Zhao, D. Dias-Da-Costa, Y. Gan, Eng. Fract. Mech. 212 (2019) 221–237.
[38] O. Mahabadi, P. Kaifosh, P. Marschall, T. Vietor, J. Rock Mech, Geotech. Eng. 6 (2014) 591–606.
[39] W. Liu, H. Deng, X. Zhu, Y. Lv, Y. Luo, Petroleum (2023), doi:10.1016/j.petlm.2023.04.002.
[40] G. Li, J. Mech. Mater. Struct. 18 (2023) 293–317.
[41] M. Tauheed, N.V. Datla, Int. J. Adhes. Adhes. 114 (2022) 103102.
[42] S. Liu, Y. Wang, C. Peng, W. Wu, Comput. Method. Appl. M. 392 (2022) 114642.
[43] D.H. Yoon, S.R. Lee, J.H. Kim, Materialwiss. Werkst. 53 (2022) 485–493.
[44] Z. Liao, Z. Yang, Q. Xue, X. Li, H. Li, W. Li, Energy Sci. Eng. 9 (2021) 772–783.
[45] X. Hao, C. Sibin, H. Yongliang, S. Xiaotong, H. Jin, C. Yuxin, J. Shandong Univ. 51 (111–118) (2021) 128.
[46] P. Li, N. Petrinic, C.R. Siviour, Mech. Mater. 54 (2012) 43–54.
[47] J. Geng, C. Liu, Constr. Build. Mater. 393 (2023) 132075.
[48] Z. Wu, X. Ji, Q. Liu, L. Fan, Comput. Geotech. 121 (2020) 103480.
[49] K.M.A.S. Bandara, P.G. Ranjith, T.D. Rathnaweera, Nat. Resour. Res. 28 (2019) 1139–1161.
[50] J.B. Parese, B.D. Jette, Single component neutrally buoyant proppant, US Patent, No. 2012/0145390, 2012.
[51] A.H. Jones, R.A. Cutler, Hollow proppants and a process for their manufacture, US Patent, No. 4574468, 1985
[52] C. Jr, J.K. Pavliscak, T.J. Wedding, C. Ann, Manufacture of strong, lightweight, hollow proppants, US Patent, No. 800675, 2011.